Ultrasensitive, fast and flexible piezoresistive strain sensor based on Te nanomesh

Yiyang Wei [a], Changyong Lan [a,*], Yu Luo [a], Fangjia Li [b,c], You Meng [d], SenPo Yip [e], Chun Li [a,*], Yi Yin [a], Johnny C. Ho [d,e,**]

[a] State Key Laboratory of Electronic Thin Films and Integrated Devices, and School of Optoelectronic Science and Engineering, University of Electronic Science and Technology of China, Chengdu 611731, China
[b] Sichuan Academy of Medical Sciences and Sichuan People's Hospital, Chengdu 610032, China
[c] School of Medicine, University of Electronic Science and Technology of China, Chengdu 611731, China
[d] Department of Materials Science and Engineering, City University of Hong Kong, Hong Kong 999077, China
[e] Institute for Materials Chemistry and Engineering, Kyushu University, Fukuoka 8168580, Japan

A B S T R A C T

Flexible, highly sensitive strain sensors operating at small strains have shown significant potential in applications such as pulsebeat detection and sound signal acquisition. In this study, we introduce ultrasensitive piezoresistive strain sensors designed to function effectively at small strains using a Te nanomesh. A large-area Te nanomesh is deposited onto a flexible polyimide substrate through physical vapor deposition, facilitating the on-site fabrication of strain sensors. The unique mesh structure imparts exceptional sensitivity to strain, achieving a remarkable gauge factor of up to 9.93×10^8. By coating the strain sensors with a thin layer of polydimethylsiloxane, we significantly enhance their stability, with minimal degradation observed even after 1000 loading-releasing cycles. The performance of these strain sensors is contingent on the mesh's density, which can be precisely controlled by adjusting the growth time of the Te nanomesh. Furthermore, our strain sensor exhibits a rapid response time of less than 4 ms, indicating its swift responsiveness. To demonstrate the superior performance of these strain sensors, we showcase their efficacy in monitoring finger bending, ruler vibrations, and sphygmus. Our findings introduce a novel design concept for flexible strain sensors and represent a significant advancement in wearable electronics and human-machine interaction technologies.

1. Introduction

Strain sensors are critical devices that convert mechanical strains into measurable electrical signals. With the rapid advancements in artificial intelligence and the Internet of Things, there is an increasing focus on developing wearable, flexible strain sensors. These sensors have potential applications in body movement tracking, medical diagnostics, human–machine interfaces, and soft robotics [1–6]. Among flexible strain sensors, various types exist, including piezoresistive, capacitive, voltage-based, and optical fiber Bragg grating sensors [7,8]. Piezoresistive strain sensors, which change resistance in response to strain, have become particularly popular for wearable healthcare diagnostics and human–machine interfaces due to their straightforward readout

mechanisms and fabrication processes [9–14].

The fabrication of flexible piezoresistive strain sensors involves depositing conductive materials onto flexible substrates, such as metal thin films, metal nanowires, carbon nanotubes, and graphene. For example, Tu et al. successfully synthesized aligned Ag nanowires/polymer composite films, arranging two films perpendicularly to create a piezoresistive strain sensor with high sensitivity, achieving a gauge factor (GF) of up to 2.98×10^6 and a working range of 200 % [15]. Building on innovative design paradigms, Bai et al. drew inspiration from bamboo slip structures to create piezoresistive strain sensors using liquid metal to modulate electrical pathways within a cracked Pt fabric electrode [16]. Their sensor exhibited remarkable attributes, including a GF exceeding 10^8 and a strain range surpassing 100 %. The impressive

performance of piezoresistive strain sensors highlights their potential across various applications and disciplines.

Despite significant advancements, traditional piezoresistive strain sensors have primarily focused on achieving high stretchability and sensitivity under extensive strains. However, high sensitivity to small strains, such as those below 1.5 %, is particularly valuable for applications like tiny skin motion detection and personal healthcare monitoring, including respiration and heartbeat [3,17]. For instance, by leveraging the intrinsic piezoresistive effect of $PdSe_2$, we developed a strain sensor capable of delivering linear responses to both compressive (−0.79 % to 0 %) and tensile (0 % to 0.79 %) strains, with GFs of 315 and − 75, respectively [18]. Chen et al. introduced a cracking-assisted piezoresistive sensor using Ag nanowires/graphene hybrid particles, achieving a GF of up to 4000 within a strain range of 0.8 % to 1 % [19]. Moreover, Gao et al. designed piezoresistive strain sensors with a unique quasi-one-dimensional conductive network, showcasing high sensitivity with a GF reaching 8.6×10^5 at a strain of 1 % [20]. While these achievements are commendable, the performance of strain sensors operating within small strain regimes remains relatively constrained compared to those under large strains. Further research is needed to enhance the capabilities of piezoresistive strain sensors in detecting and responding effectively to small-scale strains.

Piezoresistive strain sensors based on conductive networks consistently demonstrate commendable performance. For example, Amjadi et al. illustrated that a piezoresistive strain sensor, structured as a sandwich composite of an Ag nanowire network and poly-dimethylsiloxane (PDMS) elastomer, exhibited exceptional strain response [21]. Wang et al. employed a nano-engineered bilayer composed of a cracked carbon nanotube (CNT) network and an elastomer-infiltrated CNT composite to create a strain sensor with high resistance sensitivity (GF: 8–207) and a broad strain range (>50 %) [22]. However, strain sensors relying on conducting networks often display reduced sensitivity to minor strains, potentially due to the high density of the conducting network.

In previous studies, we reported the synthesis of Te nanomesh using a simple physical vapor deposition (PVD) method [23,24]. The mesh structure with controlled density may endow the structure with excellent strain-sensitive response. Consequently, we fabricated piezoresistive strain sensors based on Te nanomesh and studied their strain responses. These sensors exhibited an extraordinarily high GF of up to 9.93×10^8 at a slight strain of 1.4 %. The durability of the strain sensor can be significantly improved by coating it with a thin layer of PDMS. The performance of the strain sensors hinges on the mesh density, which can be finely adjusted by manipulating the growth time of the Te
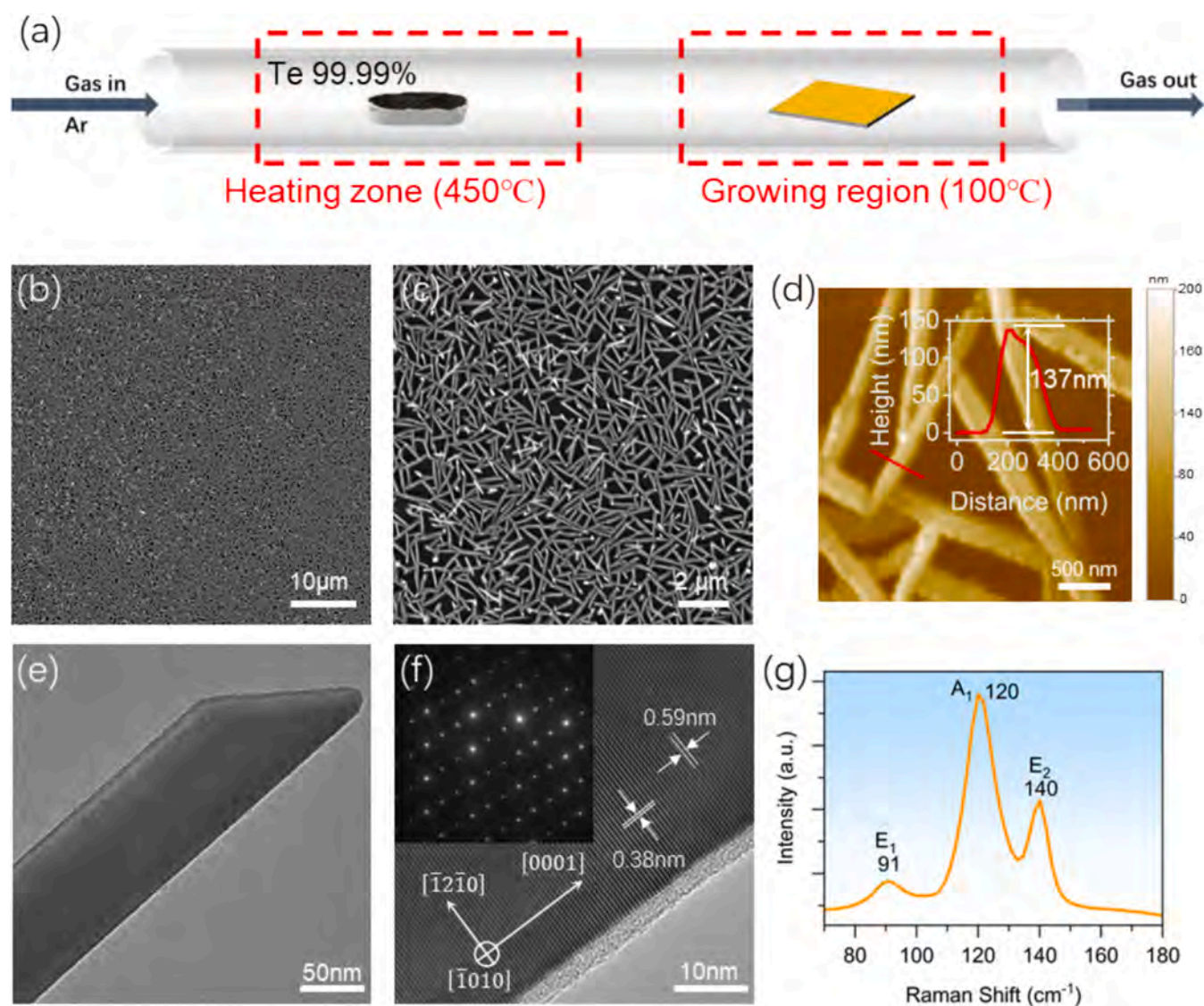

Fig. 1. Synthesis and characterization of Te nanomesh. (a) Schematic diagram of the setup for the synthesis of Te nanomesh. (b) Low magnification SEM image. (c) High magnification SEM image. (d) AFM image. (e) TEM image. (f) HRTEM image. Inset: SAED image. (g) Raman spectrum.

nanomesh. Also, the strain sensor showcases a rapid response time of less than 4 ms. Its effectiveness in monitoring finger bending, ruler vibrations, and sphygmus has been successfully demonstrated. These findings not only introduce a fresh design concept for flexible strain sensors but also signify a significant advancement in wearable electronics and human–machine interaction technologies.

2. Results and Discussion

2.1. Characterization

The Te nanomesh were synthesized on polyimide (PI) substrates via PVD at 100 °C, as schematically shown in Fig. 1a. Detailed information is provided in the experimental section. Scanning electron microscopy (SEM) images were acquired to characterize the morphology of the product using a scanning electron microscope. A typical SEM image is shown in Fig. 1b, revealing a mesh-like morphology. A high-magnification SEM image is depicted in Fig. 1c, showcasing the Te

nanowires interconnecting to form a nanomesh structure. The morphology of the Te nanomesh was further analyzed using atomic force microscopy (AFM), with a representative AFM image shown in Fig. 1d, confirming a mesh-like structure consistent with SEM observations. Crystallinity assessment of the Te nanomesh was conducted using a transmission electron microscope. Fig. 1e exhibits a typical transmission electron microscopy (TEM) image of a single Te nanowire, indicating a diameter of 100 nm. The mean diameter of the nanowires within the nanomesh is 125 nm (Fig. S1, supplementary information). A high-resolution TEM (HRTEM) image in Fig. 1f reveals clear lattice fringes, indicating the excellent crystallinity of the Te nanowire. Lattice spacings of 0.59 and 0.38 nm corresponding to the (0001) and (1000) planes, respectively, were determined, establishing the growth direction of the Te nanowire as [0001], originating from its intrinsic quasi-1D crystal structure. To further validate the high crystallinity, a selected area electron diffraction (SAED) pattern of the Te nanowire is depicted in the inset of Fig. 1f. Sharp diffraction spots are found, demonstrating the good crystallinity of the nanowire. Raman spectrum analysis in
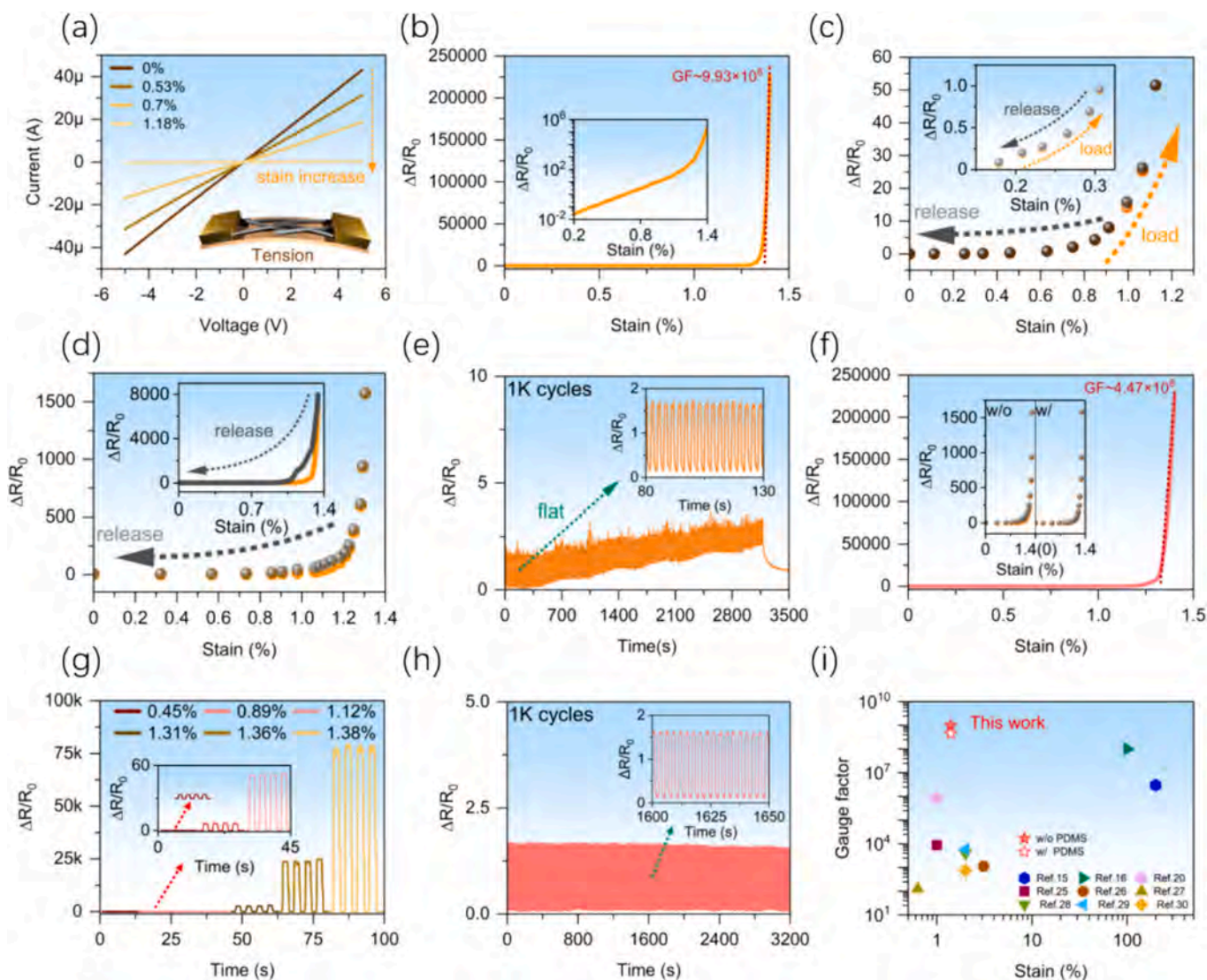

Fig. 2. Characterization of the strain sensor based on Te nanomesh. (a) Current-voltage curves of the sensor under various strains. Inset: Schematic of the device. (b) $\Delta R/R_0$ as a function of strain. Inset: Corresponding semi-log plot. (c) Loading-releasing behavior of the sensor with the maximum strain of 1.12%. Inset: Enlarged part with lower strain levels. (d) Loading-releasing behavior of the sensor with the maximum strain of 1.3%. Inset: Loading-releasing behavior with the maximum strain of 1.34%. (e) $\Delta R/R_0$ on loading-releasing cycles under a constant strain of 0.72%. Inset: Enlarged part of the stable part. (f) $\Delta R/R_0$ as a function of strain of the sensor coated with a layer of PDMS. Insets: Loading-releasing behavior with a maximum strain of 1.3%. Left – without PDMS coating, right – with PDMS coating. (g) Loading-releasing cycles under various strains. Inset: Enlarged part under small strains. (h) $\Delta R/R_0$ on Loading-releasing cycles under a constant strain of 0.72%. Inset: Enlarged part of the curve. (i) Comparison of GF with that reported in the literature [15,16,20,25–30].

Fig. 1g displays peaks at 91, 120, and 140 cm^{-1} corresponding to the E1, A1, and E2 modes of Te, respectively, affirming that the nanomesh is composed of Te. Energy dispersive X-ray spectrum (EDS) mapping, illustrated in **Fig. S2** of the supplementary information, further confirms the elementary composition of the nanomesh as Te.

2.2. Te nanomesh-based strain sensors

The strain sensors can be easily fabricated using a metal wire with a diameter of 0.6 mm as a shadow mask and depositing Ti (2.5 nm)/Au (100 nm) to serve as electrodes, creating two-terminal piezoresistive strain sensors. Detailed fabrication procedures for devices are outlined in the experimental section. An illustration of the device is provided in the inset of Fig. 2**a**, with a digital photo of a strain sensor presented in **Fig. S3a** of the supplementary information. The typical current–voltage curves of a strain sensor are displayed in Fig. 2**a**, where the linear relationship between current and applied voltage indicates an ohmic-like contact between the Te nanomesh and the electrode. Furthermore, the current gradually diminishes with increased strain, demonstrating its sensitivity. Typically, the relative change in resistance denoted as $\Delta R/R_0$, where ΔR is the resistance change under strain and R_0 is the initial resistance of the device without strain, is utilized to characterize piezoresistive strain sensors. The relative change in resistance as a function of strain is depicted in Fig. 2**b**, showcasing a significant increase in $\Delta R/R_0$ when the strain exceeds ~ 1.3 %. A semi-log plot of this curve is shown in the inset of Fig. 2**b**, clearly illustrating the noticeable resistance change in response to strain in the measured range. Typically, GF is utilized to assess the performance of the piezoresistive strain sensor, defined as

$$\text{GF} = \frac{\Delta R/R_0}{\varepsilon} \tag{1}$$

where ε represents the strain. Equation (1) is suitable for cases with a linear change in $\Delta R/R_0$ with strain. In situations where the relationship is nonlinear, the GF can be defined as

$$\text{GF} = \frac{1}{R_0} \frac{\text{d}(\Delta R)}{\text{d}\varepsilon} \tag{2}$$

According to equation (2), the strain sensor demonstrates a remarkable GF of up to 9.93×10^8, as depicted in Fig. 2**b**. Owing to the nonlinear response exhibited by the strain sensor, the GF escalates with the increase of strain, as illustrated in **Fig. S4a** of the supplementary information. The GF remains consistently high across the entire measured range of strains, showcasing the exceptional performance of the strain sensor.

The reliability of a strain sensor is paramount for its practical applications. To assess this aspect, we conducted $\Delta R/R_0$ measurements using a double strain sweep method, as presented in Fig. 2**c**. Notably, the data points corresponding to load sweeping closely align with those of release sweeping, particularly evident at lower strain levels, as highlighted in the inset of Fig. 2**c**, indicating the robust reliability of the fabricated strain sensor. However, significant deviations are observed when the maximum strain reaches 1.3 %, as illustrated in Fig. 2**d**, revealing a small hysteresis effect. With a slight increase in the maximum strain to 1.34 %, the hysteresis becomes more pronounced, as shown in the inset of Fig. 2**d**. These results suggest that hysteresis could impede practical applications despite the high GF. Given the sensor's minimal hysteresis at low strain levels, we tested its durability under a strain of 0.72 %, depicted in Fig. 2**e**. The sensor demonstrates a stable response over the initial 100 loading-releasing cycles, as indicated in the inset of the figure. However, beyond 100 cycles, the resistance no longer returns to its initial value and instead gradually increases with each successive cycle. While the resistance decreases over time upon complete strain release, it fails to recover fully within the measurement duration. Due to Te being a 1D van der Waals material, the interaction

between Te nanomesh and PI substrate relies on weak van der Waals forces. Consequently, it is plausible that the Te nanowires in the nanomesh permanently displace from their original positions during the cyclic and high-strain tests, resulting in the observed hysteresis and poor loading-releasing behavior.

To mitigate the hysteresis and reliability issues, we coated the Te nanomesh with PDMS, an elastomer, to facilitate the Te nanowires in recovering to their original positions. A digital photograph of the strain sensor with PDMS coating is shown in **Fig. S3b** of the supplementary information. The PDMS coating, with a thickness of 5 µm, is expected to leave the strain in the Te nanomesh layer unaffected. The device with the PDMS coating exhibits minimal hysteresis compared with the device without PDMS, as depicted in the inset of Fig. 2**f** and **Fig. S5** of the supplementary information. Moreover, the relative resistance changes remain consistent across various strains, suggesting that the PDMS coating does not compromise the sensor's sensitivity. The relative change of resistance within the measured strain range is displayed in Fig. 2**f**, showing a sharp increase when the strain surpasses ~ 1.3 %, akin to the observations in devices without PDMS coating. The device with PDMS also showcases a high GF of up to 4.47×10^8, comparable to the device without PDMS coating. A semi-log plot of the relative change in resistance with strain is presented in **Fig. S6** of the supplementary information, elucidating the resistance variations across the entire measured strain range. The GF versus strain curve in **Fig. S4b** of the supplementary information demonstrates an increase with strain. It should be noticed that the GF values for devices with and without PDMS differ, given that they are distinct devices despite being fabricated from the same batch of Te nanomesh. Loading-releasing tests were conducted to assess the durability of the PDMS-coated device, with results showcased in Fig. 2**g**. The $\Delta R/R_0$ response remains consistent across different strain amplitudes and increases with rising strain levels, indicating the decent stability of the device. Furthermore, a loading-releasing cyclic test was performed, illustrated in Fig. 2**h**, where the device maintains a steady response even after 1000 cycles, and can also work stably 60 cycles under extreme strain (**Fig. S7**, supplementary information), underscoring its robustness against cyclic strain pulses. As depicted in Fig. 2**i**, both the devices with PDMS and those without PDMS demonstrate higher sensitivity than the values reported in previous studies. A comprehensive comparison of the key performance parameters is presented in **Table S1** of the supplementary information, suggesting the decent performance of our devices. Additionally, we have fabricated seven more devices, all of which demonstrate similar performance, as illustrated in **Fig. S8** of the supplementary information, indicating the good reproducibility of the devices.

2.3. Operating mechanisms

Generally, there are five mechanisms for piezoresistive strain sensors [1]: geometrical effect, piezoresistive effect, tunneling effect, disconnection mechanism, and crack propagation. The geometrical effect's influence tends to be minimal, given the slight alterations in the Te conducting layer's geometry due to small strains. While Te nanowires exhibit a piezoresistive effect [31,32], their contribution alone cannot explain the remarkably high GF witnessed in our devices. The tunneling effect may impact the resistance of the device, albeit to a lesser extent. The disconnection mechanism and crack propagation are akin, delineating changes in conducting pathways under strain. The crack propagation effect typically describes continuous fragile films. In contrast, the disconnection mechanism better describes stain behavior in conductive networks, aligning more closely with the primary sensing mechanism in Te nanomesh strain sensors. In Fig. 3**a**, an SEM image of a Te nanomesh reveals both overlapped Te nanowires and self-welding Te nanowires, highlighting the coexistence of these two structural features within the nanomesh. The proposed primary strain sensing mechanism, depicted in Fig. 3**b**, models the Te nanomesh as interconnected nanowires via welding points and overlaps. Under slight strain, the reduction in
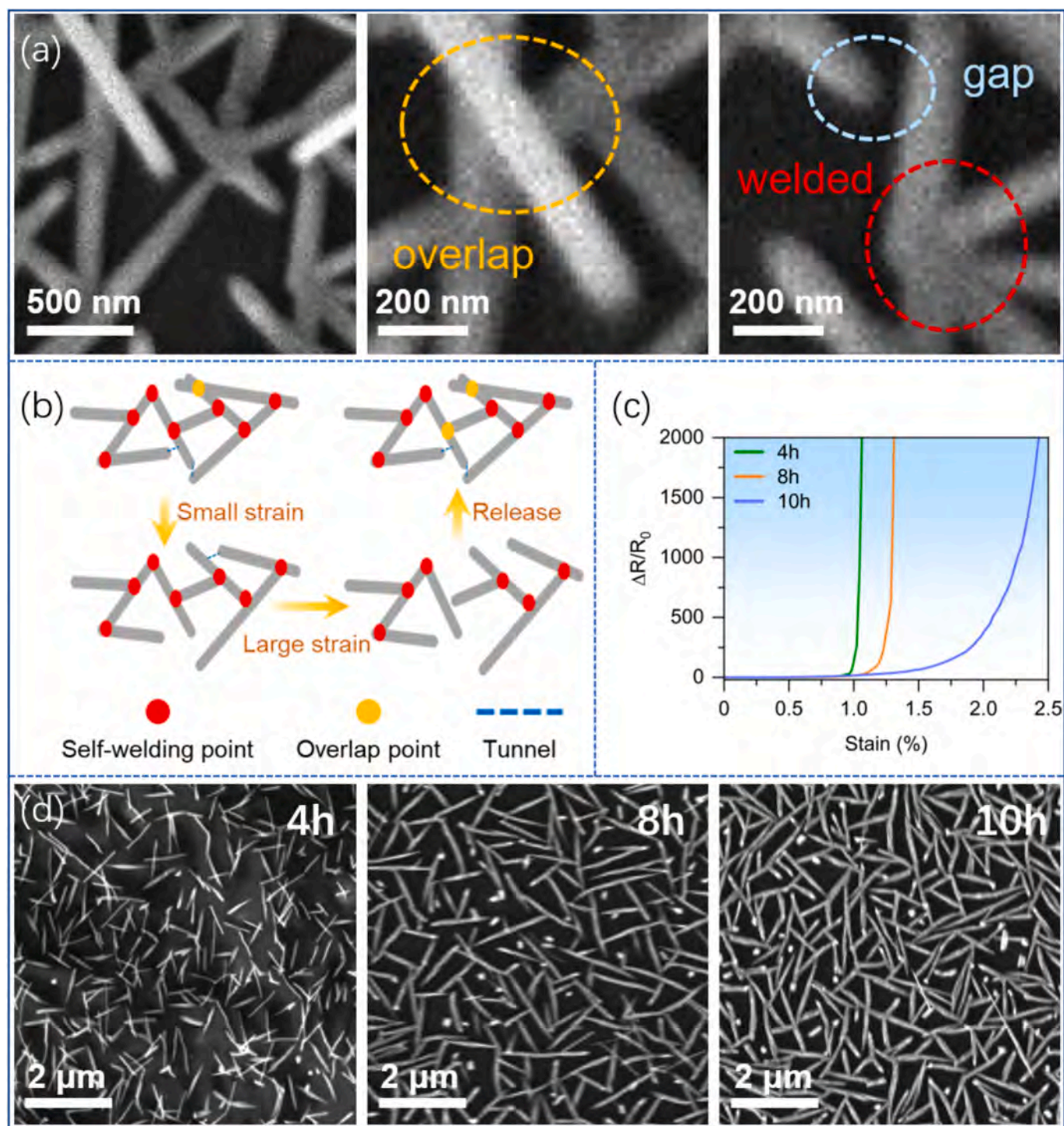
Fig. 3. Operating mechanisms. (a) SEM image of the Te nanomesh with enlarged parts showing the overlapped nanowires, the welded junction, and the small gap. (b) Schematic diagram showing the displacements of nanowires in the nanomesh during stretching and releasing. (c) Relative resistance changes of strain sensors based on Te nanomesh with various growth times. (d) SEM images of the Te nanomesh with various growth times.

conducting pathways through tunneling and nanowire overlaps leads to decreased resistance. As strain intensifies, the breaking of welding points can occur, causing a significant change in resistance and contributing to the ultra-high GF. Upon strain release, the nanomesh can revert to its initial state with the assistance of the PDMS elastomer coating. According to the proposed mechanism, the response of the strain sensor can be tailored by adjusting the nanowire density in the Te nanomesh. Fig. 3c illustrates that the critical strain for a significant increase in $\Delta R/R_0$ rises with longer growth times of the Te nanomesh. The

SEM image in Fig. 3d reveals that nanowire density increases with extended growth times, augmenting conducting pathways. Consequently, a higher critical strain is required for welding point breakage, which aligns with the findings in Fig. 3c. Moreover, employing Te nanomesh with higher densities expands the strain range while sacrificing sensitivity. Additionally, the critical strain can be finely adjusted by slightly increasing the growth time of the Te nanomesh, as demonstrated in Fig. S9 of the supplementary information. To confirm the proposed mechanism, we fitted the $\Delta R/R_0$ versus strain curves using a

model that considers only tunneling between nanowires and changes in conductive pathways, as detailed in **Note 1** and **Fig. S10** of the supplementary information. The excellent agreement between the model and the measured curves validates the proposed sensing mechanism. Additionally, simulations based on the proposed mechanism were conducted, as shown in **Note 2** and **Fig. S11** of the supplementary information. The close match between experimental and simulation results further supports the validity of the proposed mechanisms. Moreover, SEM image of the Te nanomesh under a large strain (1.13 %) (**Fig. S12**, supplementary information) clearly shows the breaking of welding points and the separation of nanowires, providing direct evidence for the proposed mechanism.

2.4. Applications

Given the ultra-high sensitivity of the strain sensors, their preliminary applications have been demonstrated. In **Fig. 4a**, the response of the Te nanomesh strain sensor to finger bending is illustrated. The inset of **Fig. 4a** displays a schematic of the device mounted on a finger. The sensor's resistance varies with various bending angles while maintaining stable values, indicating potential for finger gesture recognition. For instance, by defining small angle bending as "•" and large bending angle as "-", and encoding characters using these symbols as depicted in **Fig. 4b**, the codes can be converted into electrical signals through finger bending. The characters can then be easily deciphered from these electrical signals, as shown in **Fig. 4c**. Moreover, our strain sensor can also be utilized to monitor the vibration of a ruler, with the experimental setup schematically presented in **Fig. 4d**. The recorded resistance over time during multiple vibrations of the ruler is displayed in **Fig. 4d**, revealing significant resistance change peaks. **Fig. 4e** showcases an enlarged portion of a single pulse, which contains multiple sub-pulses corresponding to the damped vibrations of the ruler. The well-traced damped vibrations highlight the strain sensor's high sensitivity and rapid response. In **Fig. 4e**, the rise time is employed to estimate the sensor's response time, which is approximately 4 ms. However, the actual

response time is anticipated to be even shorter. Leveraging its high sensitivity and quick response, the sensor was further employed to monitor arterial pulses in the human body, as depicted in the left inset of **Fig. 4f**. The recorded signal, shown in **Fig. 4f**, illustrates arterial pulse peaks in resistance. Pulse rates of approximately 86 beats/min can be derived from the curve. Additionally, the right inset of **Fig. 4f** magnifies a section of the curve showing a single pulse, where three distinct subpeaks representing the percussion wave (P-wave), tidal wave (T-wave), and diastolic wave (D-wave) are identifiable. Furthermore, the device was used to measure arterial pulses in individuals of varying ages and genders, showcasing differences in pulse signals across demographic groups, highlighting the practical application value of the device (**Fig. S13**, supplementary information).

The real-time monitoring of physiological signals plays a crucial role in predicting, diagnosing, and treating various diseases. This objective can be achieved through a wireless wearable sensor network platform, illustrated schematically in **Fig. 5a**. To showcase the potential of our strain sensors in such applications, we developed a wireless real-time monitoring system based on the Arduino platform, depicted in **Fig. 5b**. Our strain sensor effectively captures arterial pulse signals gathered by the platform, transmitted to a personal computer or smartphone, and displayed on a screen, as depicted in **Fig. 5c**. These outcomes concerning Te nanomesh piezoresistive strain sensors indicate their commendable performance and promise for integration into wireless wearable devices.

3. Conclusions

In conclusion, we successfully demonstrated the capabilities of flexible Te nanomesh strain sensors, showcasing ultra-high sensitivity and rapid response speed. These two-terminal piezoresistive strain sensors were created by depositing electrodes onto Te nanomesh grown on PI flexible substrate using PVD. Notably, the strain sensor displayed an extraordinary GF of 9.93×10^8. To enhance the durability of the strain sensor, PDMS was employed, enabling the sensor to maintain a stable response even after 1000 loading-releasing cycles. The primary
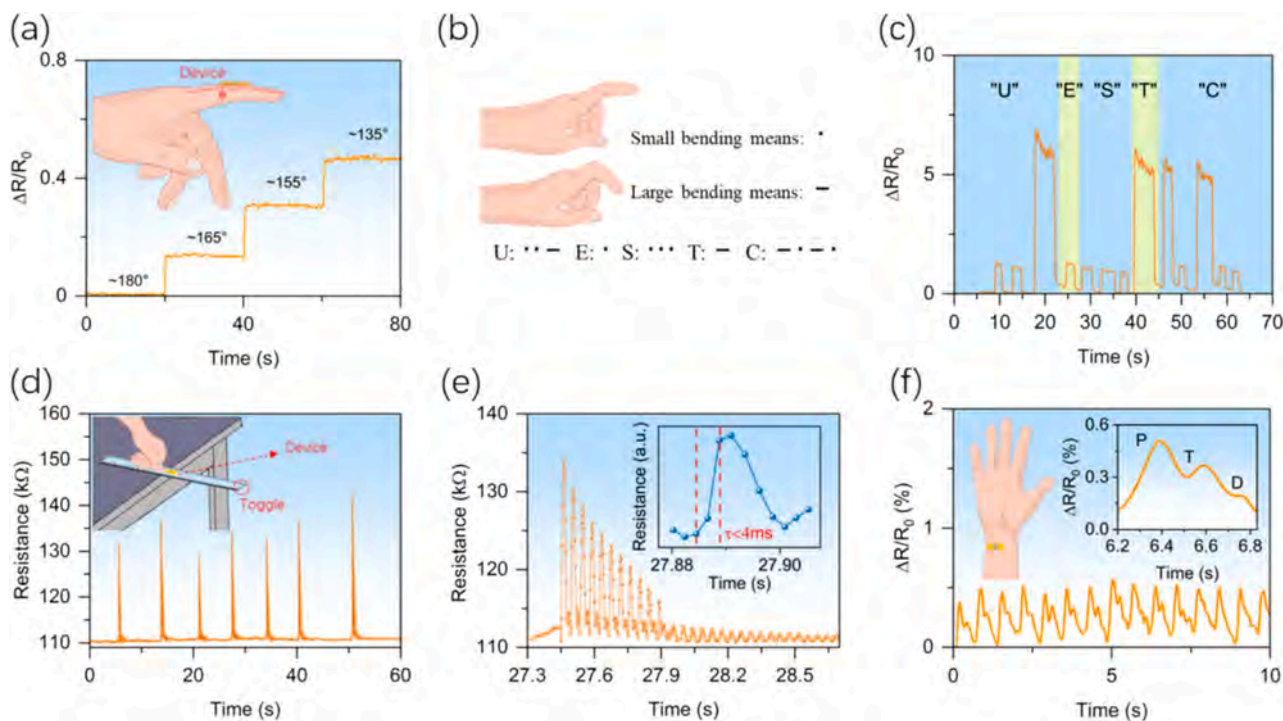

Fig. 4. Applications. Monitor finger bending. (a) Schematic of finger bending and the corresponding responses. (b) Schematic of Coding by finger bending. (c) coding signal. Vibration monitor. (d) Schematic of the vibration monitor and corresponding signals. (e) Time-resolved response. Inset: Enlarged part of the curve. Sphygmus monitor. (f) Schematic and corresponding signal. Inset: Enlarged part of the curve.
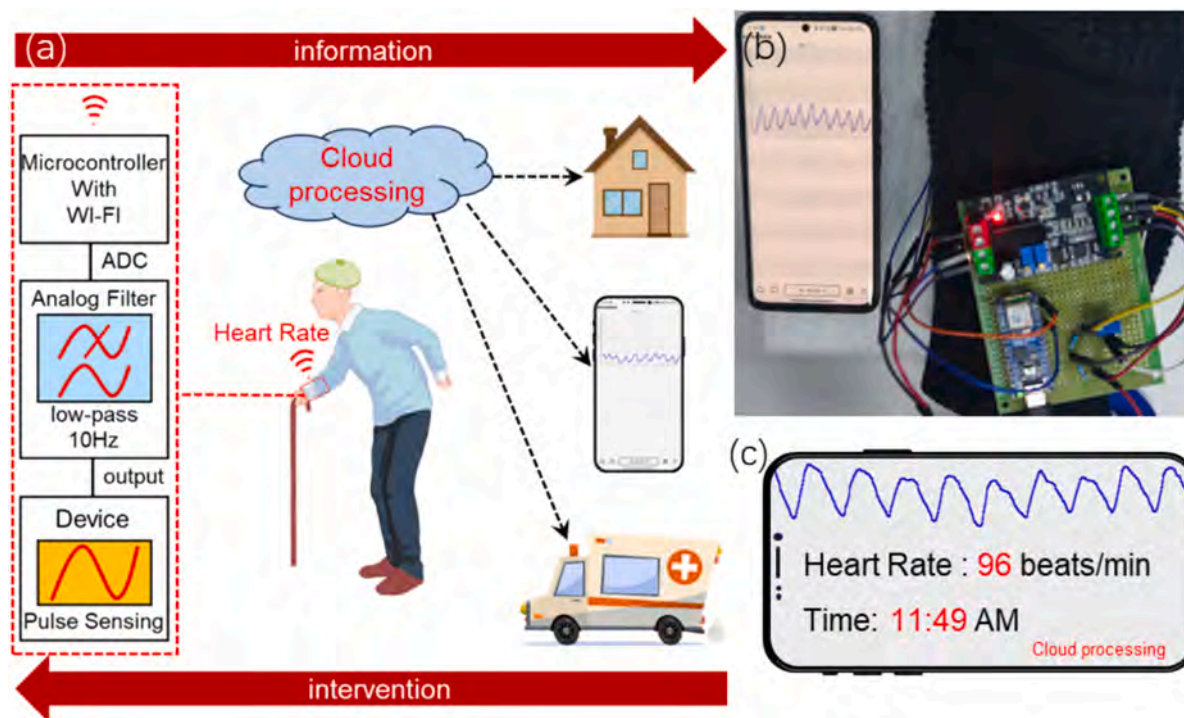
Fig. 5. Wireless Realtime Sphygmus monitor. (a) Schematic of the system. (b) Digital photograph of the real-time test. (c) The monitor results.

reason behind the remarkable sensitivity of these sensors was linked to alterations in conducting pathways under strain. The critical strain necessary for a significant increase in resistance was found to be dependent on the density of the Te nanowire within the nanomesh structure. The strain sensors proved effective in monitoring activities such as finger bending, ruler vibrations, and arterial pulses, showcasing their exceptional performance. Furthermore, we successfully implemented a wireless real-time arterial pulse monitoring system utilizing our strain sensor. Our findings underscore the significant role of Te nanomesh in strain sensing applications and offer a straightforward approach for fabricating high-performance piezoresistive strain sensors.

4. Experimental section

4.1. Synthesis of Te nanomesh

A 200 μm thick layer of polyimide (PI) served as the substrate for synthesizing Te nanomesh. The synthesis occurred within a two-zone horizontal tube furnace featuring a 1-inch diameter quartz tube under atmospheric pressure conditions. The PI substrate was carefully positioned in the low-temperature heating zone (100 °C), while 1 g of Te powder (99.99 %) was situated in the high-temperature heating zone (450 °C). Before heating, the quartz tube was purged with argon gas with a flow rate of 300 sccm to remove oxygen from the system. Subsequently, argon gas with a flow rate of 15 sccm was introduced into the tube furnace, and the heating process was initiated. The typical deposition time was 8 h. After the deposition, a dense Te nanomesh was formed on the surface of the PI substrate.

4.2. Characterization

The Raman spectra of the Te nanomesh were acquired using a Raman spectrometer (SR-5001-A-R, Andor) with a 532 nm laser as the excitation source. SEM images were obtained using a scanning electron microscope (VEGA3 SBH, TESCAN). EDS mapping was performed in the SEM using the EDS accessory (XFlash SCU Gen 7, Bruker) on the scanning electron microscope. AFM images were obtained using an atomic

force microscope (NX10, Park). TEM and HRTEM images were obtained using a transmission electron microscope (F200S G2, Talos).

4.3. Device fabrication

A copper wire with a diameter of 0.6 mm was used as a shadow mask to define the channel length between electrodes. Ti (2.5 nm) and Au (100 nm) were sequentially deposited on the copper wire masked Te nanomesh by e-beam evaporation to form a two-terminal strain sensor.

4.4. Measurements of strain responses

The tests were carried out in a motorized one-dimensional displacement stage, as shown in **Fig. S14**a, supplementary information. The strain in the Te nanomesh layer was calculated according to $h/2r$, where h is the thickness of the PI film, and r is the bending radius, as schematically shown in **Fig. S14**b, supplementary information. The device's electrical properties were measured by a semiconductor analyzer (B1500A, Keysight) and a measurement-and-source unit (B2902A, Keysight). A wireless real-time strain response monitoring system was fabricated using the Arduino platform (nano esp32), including a processing and transmission module and a denoising and amplifying module, as shown in **Fig. S15**, supplementary information.

CRediT authorship contribution statement

Yiyang Wei: Writing – original draft, Visualization, Validation, Methodology, Investigation, Formal analysis, Data curation. **Changyong Lan:** Writing – review & editing, Writing – original draft, Project administration, Methodology, Funding acquisition, Formal analysis, Conceptualization. **Yu Luo:** Visualization, Methodology, Investigation. **Fangjia Li:** Methodology, Investigation. **You Meng:** Methodology, Investigation. **SenPo Yip:** Methodology, Formal analysis. **Chun Li:** Resources, Funding acquisition, Formal analysis. **Yi Yin:** Funding acquisition, Formal analysis. **Johnny C. Ho:** Writing – review & editing, Formal analysis.

Declaration of competing interest

The authors declare that they have no known competing financial interests or personal relationships that could have appeared to influence the work reported in this paper.

Acknowledgements

Appendix A. Supplementary data

Supplementary data to this article can be found online at https://doi.org/10.1016/j.cej.2025.162024.

Data availability

Data will be made available on request.

References

[1] H. Chen, F.L. Zhuo, J. Zhou, Y. Liu, J.B. Zhang, S.R. Dong, X.Q. Liu, A. Elmarakbi, H.G. Duan, Y.Q. Fu, Advances in graphene-based flexible and wearable strain sensors, Chem. Eng. J. 464 (2023) 142576, https://doi.org/10.1016/j.cej.2023.142576.

[2] T. Nguyen, T. Dinh, H.P. Phan, T.A. Pham, V.T. Dau, N.T. Nguyen, D.V. Dao, Advances in ultrasensitive piezoresistive sensors: from conventional to flexible and stretchable applications, Mater. Horiz. 8 (2021) 2123–2150, https://doi.org/10.1039/d1mh00538c.

[3] L.Y. Duan, D.R. D'Hooge, L. Cardon, Recent progress on flexible and stretchable piezoresistive strain sensors: From design to application, Prog. Mater. Sci. 114 (2020) 100617, https://doi.org/10.1016/j.pmatsci.2019.100617.

[4] H. Souri, H. Banerjee, A. Jusufi, N. Radacsi, A.A. Stokes, I. Park, M. Sitti, M. Amjadi, Wearable and Stretchable Strain Sensors: Materials, Sensing Mechanisms, and Applications, Adv. Intell. Syst. 2 (2020) 2000039, https://doi.org/10.1002/aisy.202000039.

[5] D. Rus, M.T. Tolley, Design, fabrication and control of soft robots, Nature 521 (2015) 467–475, https://doi.org/10.1038/nature14543.

[6] Y.Z. Bai, L.T. Yin, C. Hou, Y.L. Zhou, F. Zhang, Z.Y. Xu, K. Li, Y.A. Huang, Response Regulation for Epidermal Fabric Strain Sensors via Mechanical Strategy, Adv. Funct. Mater. 33 (2023) 2214119, https://doi.org/10.1002/adfm.202214119.

[7] A.D. Qiu, P.L. Li, Z.K. Yang, Y. Yao, I. Lee, J. Ma, A Path Beyond Metal and Silicon: Polymer/Nanomaterial Composites for Stretchable Strain Sensors, Adv. Funct. Mater. 29 (2019) 1806306, https://doi.org/10.1002/adfm.201806306.

[8] Y.Y. Si, S.J. Chen, M. Li, S.Y. Li, Y.S. Pei, X.J. Guo, Flexible Strain Sensors for Wearable Hand Gesture Recognition: From Devices to Systems, Adv. Intell. Syst. 4 (2022) 2100046, https://doi.org/10.1002/aisy.202100046.

[9] J.C. Yang, J. Mun, S.Y. Kwon, S. Park, Z.N. Bao, S. Park, Electronic Skin: Recent Progress and Future Prospects for Skin-Attachable Devices for Health Monitoring, Robotics, and Prosthetics, Adv. Mater. 31 (2019) 1904765, https://doi.org/10.1002/adma.201904765.

[10] B. Shih, D. Shah, J.X. Li, T.G. Thuruthel, Y.L. Park, F. Iida, Z.A. Bao, R. Kramer-Bottiglio, M.T. Tolley, Electronic skins and machine learning for intelligent soft robots, Sci. Rob. 5 (2020) eaaz9239, https://doi.org/10.1126/scirobotics.aaz9239.

[11] Y. Wang, S. Lee, T. Yokota, H.Y. Wang, Z. Jiang, J.B. Wang, M. Koizumi, T. Someya, A durable nanomesh on-skin strain gauge for natural skin motion monitoring with minimum mechanical constraints, Sci. Adv. 6 (2020) eabb7043, https://doi.org/10.1126/sciadv.abb7043.

[12] C. Wei, W.S. Lin, L. Wang, Z.C. Cao, Z.J. Huang, Q.L. Liao, Z.Q. Guo, Y.H. Su, Y.J. Zheng, X.Q. Liao, Z. Chen, Conformal Human-Machine Integration Using Highly Bending-Insensitive, Unpixelated, and Waterproof Epidermal Electronics Toward Metaverse, Nano-Micro Lett. 15 (2023) 199, https://doi.org/10.1007/s40820-023-01176-5.

[13] J.W. Chen, F. Wang, G.X. Zhu, C.B. Wang, X.H. Cui, M. Xi, X.H. Chang, Y.T. Zhu, Breathable Strain/Temperature Sensor Based on Fibrous Networks of Ionogels

Capable of Monitoring Human Motion, Respiration, and Proximity, ACS Appl. Mater. Interfaces 13 (2021) 51567–51577, https://doi.org/10.1021/acsami.1c16733.

[14] J.Y. Li, Q.L. Ding, H. Wang, Z.X. Wu, X.C. Gui, C.W. Li, N. Hu, K. Tao, J. Wu, Engineering Smart Composite Hydrogels for Wearable Disease Monitoring, Nano-Micro Lett. 15 (2023) 105, https://doi.org/10.1007/s40820-023-01079-5.

[15] S.H. Tu, Y. Ma, L. Shi, H. Li, M. Chen, L.M. Wu, Aligned silver Nanowires/Polymer composite films for ultrasensitive and highly stretchable strain sensors, Chem. Eng. J. 473 (2023) 145075, https://doi.org/10.1016/j.cej.2023.145075.

[16] Y.Z. Bai, Y.L. Zhou, X.Y. Wu, M.F. Yin, L.T. Yin, S.Y. Qu, F. Zhang, K. Li, Y.A. Huang, Flexible Strain Sensors with Ultra-High Sensitivity and Wide Range Enabled by Crack-Modulated Electrical Pathways, Nano-Micro Lett. 17 (2025) 64, https://doi.org/10.1007/s40820-024-01571-6.

[17] D. Kang, P.V. Pikhitsa, Y.W. Choi, C. Lee, S.S. Shin, L.F. Piao, B. Park, K.Y. Suh, T.I. Kim, M. Choi, Ultrasensitive mechanical crack-based sensor inspired by the spider sensory system, Nature 516 (2014) 222–226, https://doi.org/10.1038/nature14002.

[18] R. Zhang, J. Lin, T. He, J.F. Wu, Z.J. Yang, L.W. Liu, S.F. Wen, Y.M. Gong, H.F. Lv, J. Zhang, Y. Yin, F.J. Li, C.Y. Lan, C. Li, High-performance piezoresistive sensors based on transfer-free large-area PdSe$_2$ films for human motion and health care monitoring, InfoMat 6 (2024) e12484, https://doi.org/10.1002/inf2.12484.

[19] S. Chen, Y. Wei, S.M. Wei, Y. Lin, L. Liu, Ultrasensitive Cracking-Assisted Strain Sensors Based on Silver Nanowires/Graphene Hybrid Particles, ACS Appl. Mater. Interfaces 8 (2016) 25563–25570, https://doi.org/10.1021/acsami.6b09188.

[20] Z.Y. Gao, D. Xu, S.B. Li, D.D. Zhang, Z.Y. Xiang, H.F. Zhang, Y.Z. Wu, Y.W. Liu, J. Shang, R.W. Li, Quasi-1D Conductive Network Composites for Ultra-Sensitive Strain Sensing, Adv. Sci. 2403635 (2024), https://doi.org/10.1002/advs.202403635.

[21] M. Amjadi, A. Pichitpajongkit, S. Lee, S. Ryu, I. Park, Highly Stretchable and Sensitive Strain Sensor Based on Silver Nanowire-Elastomer Nanocomposite, ACS Nano 8 (2014) 5154–5163, https://doi.org/10.1021/nn501204t.

[22] Y. Wang, F. Wang, S. Yazigi, D.X. Zhang, X.C. Gui, Y.Z. Qi, J. Zhong, L. Sun, Nanoengineered highly sensitive and stable soft strain sensor built from cracked carbon nanotube network/composite bilayers, Carbon 173 (2021) 849–856, https://doi.org/10.1016/j.carbon.2020.11.025.

[23] Y. Meng, X.C. Li, X.L. Kang, W.P. Li, W. Wang, Z.X. Lai, W.J. Wang, Q. Quan, X.M. Bu, S. Yip, P.S. Xie, D. Chen, D.J. Li, F. Wang, C.F. Yeung, C.Y. Lan, C.T. Liu, L.F. Shen, Y. Lu, F.R. Chen, C.Y. Wong, J.C. Ho, Van der Waals nanomesh electronics on arbitrary surfaces, Nat. Commun. 14 (2023) 2431, https://doi.org/10.1038/s41467-023-38090-8.

[24] Y.Y. Wei, C.Y. Lan, J. Zeng, Y. Meng, S.R. Zhou, S. Yip, C. Li, Y. Yin, J.C. Ho, Te nanomesh/black-Si van der Waals Heterostructure for High-Performance Photodetector, Adv. Opt. Mater. 12 (2024) 2400056, https://doi.org/10.1002/adom.202400056.

[25] T.S.D. Le, J.N. An, Y. Huang, Q. Vo, J. Boonruangkan, T. Tran, S.W. Kim, G.Z. Sun, Y.J. Kim, Ultrasensitive Anti-Interference Voice Recognition by Bio-Inspired Skin-Attachable Self-Cleaning Acoustic Sensors, ACS Nano 13 (2019) 13293–13303, https://doi.org/10.1021/acsnano.9b06354.

[26] Y.F. Hu, T.Q. Huang, H.J. Zhang, H.J. Lin, Y. Zhang, L.W. Ke, W. Cao, K. Hu, Y. Ding, X.Y. Wang, K. Rui, J.X. Zhu, W. Huang, Ultrasensitive and Wearable Carbon Hybrid Fiber Devices as Robust Intelligent Sensors, ACS Appl. Mater. Interfaces 19 (2021) 23905–23914, https://doi.org/10.1021/acsami.1c03615.

[27] C.B. Huang, Y.F. Yao, V. Montes-García, M.A. Stoeckel, M. Von Holst, A. Ciesielski, P. Samorì, Highly Sensitive Strain Sensors Based on Molecules-Gold Nanoparticles Networks for High-Resolution Human Pulse Analysis, Small 17 (2021) 2007593, https://doi.org/10.1002/smll.202007593.

[28] T. Lee, Y.W. Choi, G. Lee, P.V. Pikhitsa, D. Kang, S.M. Kim, M. Choi, Transparent ITO mechanical crack-based pressure and strain sensor, J. Mater. Chem. C 4 (2016) 9947–9953, https://doi.org/10.1039/c6tc03329f.

[29] Z.W. Han, L.P. Liu, J.Q. Zhang, Q.G. Han, K.J. Wang, H.L. Song, Z. Wang, Z.B. Jiao, S.C. Niu, L.Q. Ren, High-performance flexible strain sensor with bio-inspired crack arrays, Nanoscale 10 (2018) 15178–15186, https://doi.org/10.1039/c8nr02514b.

[30] Y.C. Qiao, H. Tang, H.D. Liu, J.M. Jian, S.R. Ji, F. Han, Z.Y. Liu, Y. Liu, Y.F. Li, T.R. Cui, J.X. Cai, G.Y. Gou, B.P. Zhou, Y. Yang, T.L. Ren, J.H. Zhou, Intelligent and highly sensitive strain sensor based on indium tin oxide micromesh with a high crack density, Nanoscale 14 (2022) 4234–4243, https://doi.org/10.1039/d1nr08005a.

[31] S. Dang, S.D. Kang, T. Dai, X.Y. Ma, H.W. Li, W.Q. Zhou, G.L. Wang, P. Hu, Y. Sun, Z.H. He, F.M. Yu, X. Zhou, S.X. Wu, S.W. Li, Piezoelectric modulation of broadband photoresponse of flexible tellurium nanomesh photodetectors, Nanotechnology 31 (2020) 095502, https://doi.org/10.1088/1361-6528/ab53b3.

[32] S.J. Ran, T.S. Glen, B. Li, T.Y. Zheng, I.S. Choi, S.T. Boles, Mechanical Properties and Piezoresistivity of Tellurium Nanowires, J. Phys. Chem. C 123 (2019) 22578–22585, https://doi.org/10.1021/acs.jpcc.9b05597.